Kim et al. *NPG Asia Materials* (2024) 16:59
https://doi.org/10.1038/s41427-024-00578-0

NPG Asia Materials

ARTICLE Open Access

Molecular beam epitaxial In_2Te_3 electronic devices

Imhwan Kim[1], Jinseok Ryu[2], Eunsu Lee[1], Sangmin Lee[2], Seokje Lee[1], Wonwoo Suh[1], Jamin Lee[3], Miyoung Kim[2], Hong seok Oh[4] and Gyu-Chul Yi[1]

Abstract

We report on the electrical characteristics of field-effect transistors (FETs) and Schottky diodes based on In_2Te_3 grown on hexagonal boron nitride (*h*-BN) substrates utilizing molecular beam epitaxy (MBE). A two-step growth method was used to increase surface coverage and large grain sizes for high-quality In_2Te_3. Scanning transmission electron microscopy (STEM) imaging revealed an atomically clean and abrupt interface between the In_2Te_3 and *h*-BN substrates. Compared with the previously reported In_2Te_3 FETs, the MBE-grown In_2Te_3 FETs exhibited superior electrical properties, including a mobility of 6.07 $cm^2 V^{-1} s^{-1}$, a subthreshold swing close to 6 V dec^{-1}, and an impressive on/off ratio of approximately 10^5. Furthermore, the Ti/In_2Te_3 Schottky diodes exhibit a low saturation current of 0.4 nA, an ideality factor of 26.7, and a Schottky barrier height of 0.68 eV.

Introduction

Recently, there has been increasing interest in the preparation and characterization of group III-VI chalcogenide semiconductor material-based electronic and optoelectronic device applications[1–11]. Among these materials, In_2Te_3 stands out as a narrow-band gap semiconductor with diverse applications in superconductors, optoelectronics, and electronic devices. For these applications, high-quality In_2Te_3 thin films are necessary. However, achieving high-quality In_2Te_3 films remains challenging despite the use of methods such as chemical vapor deposition (CVD) and pulsed laser deposition (PLD)[12,13]. The variable stoichiometries of indium telluride (e.g., In_2Te_3, InTe, In_4Te_3, and In_7Te_{10}) complicate composition control[11,12,14,15], posing significant obstacles to the preparation of high-quality In_2Te_3 films.

Here, molecular beam epitaxy (MBE) was employed to achieve precise control over the composition and phase, enabling the production of high-quality In_2Te_3 thin films. In this study, we report on the fabrication and characterization of MBE-grown In_2Te_3 field-effect transistors (FETs) and Schottky diodes.

Correspondence: Gyu-Chul Yi (gcyi@snu.ac.kr)
[1]Department of Physics and Astronomy, Institute of Applied Physics, Seoul National University, Seoul, South Korea
[2]Department of Material Science Engineering and Research Institute of Advanced Materials, Seoul National University, Seoul, South Korea
Full list of author information is available at the end of the article

Materials and methods

In_2Te_3 growth using MBE

In_2Te_3 thin films were grown on hexagonal boron nitride (*h*-BN) substrates using a custom-built MBE (Fig. S1) system for the growth of $(In_xGa_{1-x})_2(Se_yTe_{1-y})_3$ materials. The chamber base pressure of the MBE system was low at 10^{-9} Torr. The *h*-BN layers were mechanically exfoliated onto a Si wafer covered with 300 nm-thick SiO_2 for substrate preparation. High-purity indium and tellurium fluxes were evaporated by Knudsen cells. The Te/In beam flux ratio was 14–16 for the growth. Before the 1st step of growth, a thermal cleaning process was conducted for 20 min at 500 °C under ultrahigh vacuum (UHV) conditions before the growth of In_2Te_3. First, the 1st step of growth was performed at 270 °C for 4 min. After this, the indium Knudsen cell shutter was closed, and the substrate temperature gradually increased to 570 °C at a rate of 10 °C per minute with tellurium flux. Further, the second step of growth was conducted at 570 °C for 9 min, after which the indium shutter was closed. The substrate temperature was subsequently decreased to room temperature at a rate of 10 °C per minute with tellurium flux. Finally, the substrate shutter was closed at 500 °C.

Optical characterization

A micro-Raman system was used to measure samples in ambient air at room temperature utilizing an ~150 μW,

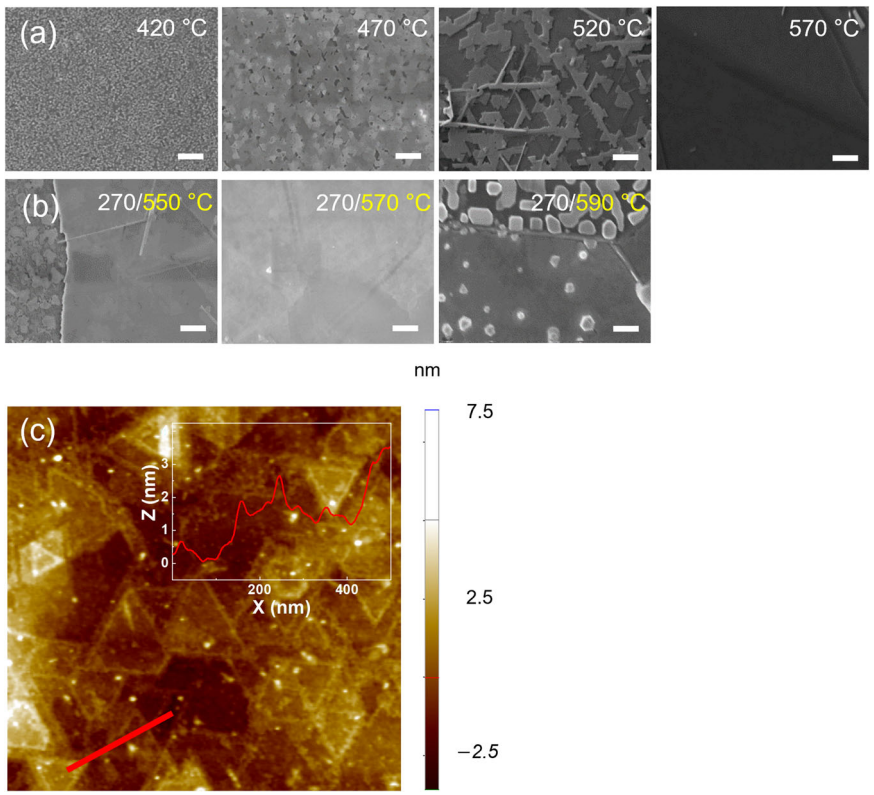

Fig. 1 Surface morphology of MBE-grown In_2Te_3 thin films on *h*-BN layers. a SEM images of one-step-grown films at different growth temperatures of 420, 470, 520, and 570 °C, respectively. **b** SEM images of two-step-grown films with initial deposition at 270 °C and second-step growth at 550, 570, and 590 °C, respectively. **c** AFM image of In_2Te_3 grown on *h*-BN. AFM line profile obtained across the red line in the main figure shown in the inset in **c**. The Scale bar for the inset is 200 nm.

532 nm laser. To acquire the Raman spectra, an accumulation time of 20 s was used.

Surface morphological and structural characterization

To study the surface morphology of In_2Te_3 films on *h*-BN substrates, field-emission scanning electron microscopy (SEM) (ZEISS-SUPRA, SIGMA, MERLIN COMPACT) and atomic force microscopy (AFM) (NX-10) were used. A 200 kV CS-corrected monochromatic transmission electron microscope (TEM) (Themis Z) was used for high-resolution scanning transmission electron microscopy (HR-STEM) imaging.

Device fabrication

Initially, *h*-BN layers were placed on a SiO_2/Si wafer, which acted as the back gate dielectric material and electrode, respectively. The MBE method was subsequently used to grow In_2Te_3 on *h*-BN substrates. Using an *e*-beam evaporator, an array of aligner markers (Ti/Au 10/30 nm) were deposited. For the ohmic contacts and Schottky contacts, Pd/Au 10/30 nm and Ti/Au 10/30 nm materials were deposited using an *e*-beam evaporator. The negative *e*-beam resist ma-N 2405 (microresist technology) layer was spin-coated (1000/4000 rpm 10/60 s). For patterning the ma-N 2405 layer, *e*-beam lithography was used. Unwanted In_2Te_3 films were then etched using reactive ion etching with Cl_2 gas. The electrical measurements were carried out in a Keithley 4200 semiconductor analyzer with 2601 A and 2400 source meters.

Results and Discussion

To study growth behavior, the surface morphology of the In_2Te_3 thin films were investigated at various growth temperatures, which ranged from 420 °C to 570 °C (Fig. 1a). Facets were absent at a lower growth temperature of 420 °C but became discernible as the temperature increased. The domain sizes expand from several tens of nanometers (at 470 °C) to several hundreds of nanometers (at 520 °C), suggesting that higher temperatures lead to larger terraces and smoother surfaces. However, no growth was observed at 570 °C, which can make uniform thin film formation difficult for electrical applications, primarily due to the lack of dangling bonds on *h*-BN, as previously reported[16].

A two-step growth strategy was adopted to address this issue, enhancing the number of nucleation sites at lower

temperatures before proceeding to higher temperatures for full-coverage film growth. Initially, at a low temperature, the first growth step aimed to ensure nearly complete surface coverage. Following this, while the substrate temperature was gradually increased, the films were annealed under tellurium flux for several minutes. This approach effectively addresses the challenges posed by the inert nature of *h*-BN at high temperatures, increasing the number of nucleation sites and preventing film texturing. The effectiveness of this two-step growth approach is depicted in the surface morphologies of the films grown at various second step temperatures, as illustrated in Fig. 1b. Since the films that nucleated below this temperature maintained island structures even after high-temperature annealing, 270 °C was chosen as the growth temperature for the first step. For the second step, higher temperatures of 550 °C and 570 °C led to a flat and uniform surface morphology. However, at temperatures of approximately 590 °C, the surface coverage decreased, likely due to the re-evaporation of the In_2Te_3 films. Based on these observations, the optimal temperatures for the first and second steps were established at 270 °C and 550–570 °C, respectively.

AFM was employed to obtain atomic-scale surface information on the In_2Te_3 films. AFM analysis revealed smooth terraces spanning an area of over 200 nm, indicative of desirable growth behavior that produces atomically smooth films (Fig. 1c). Additionally, the AFM image displayed well-defined crystal facets in each domain, with a root mean square (RMS) roughness of 1.4 nm.

The atomic arrangement and interfacial quality of In_2Te_3/*h*-BN were analyzed using HR-STEM. Cross-sectional HR-STEM imaging revealed a thickness of In_2Te_3 ~ 12.2 ± 0.2 nm (the inset of Fig. 2a) and a clean interface between In_2Te_3 and *h*-BN, free of any interfacial layers, cracks, or dislocations, with In_2Te_3 exhibiting well-aligned growth directions parallel to the *h*-BN substrate (Fig. 2a). The composition at the interface was determined using TEM-energy dispersive X-ray spectroscopy (EDS) mapping, revealing atomic percentages of 40.2% indium and 59.8% tellurium, which is consistent with the stoichiometric composition of In_2Te_3, as depicted in Fig. 2b. Further stoichiometric characterization was conducted using Raman spectroscopy. As detailed in Fig. S1, three prominent peaks were identified at 104, 125, and 142 cm^{-1}. These peaks are characteristic of In_2Te_3 crystal symmetry and specifically correspond to the A_{1g} and E_g vibrational modes, respectively. These peaks highly correspond to In_2Te_3. These results are consistent with those in Fig. 2b. This precise control of composition underscores the benefits of using MBE to maintain a clean interface.

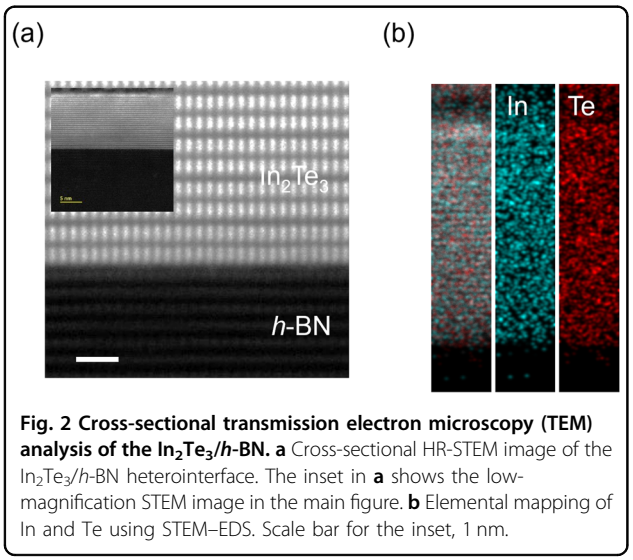

Fig. 2 Cross-sectional transmission electron microscopy (TEM) analysis of the In_2Te_3/*h*-BN. a Cross-sectional HR-STEM image of the In_2Te_3/*h*-BN heterointerface. The inset in **a** shows the low-magnification STEM image in the main figure. **b** Elemental mapping of In and Te using STEM–EDS. Scale bar for the inset, 1 nm.

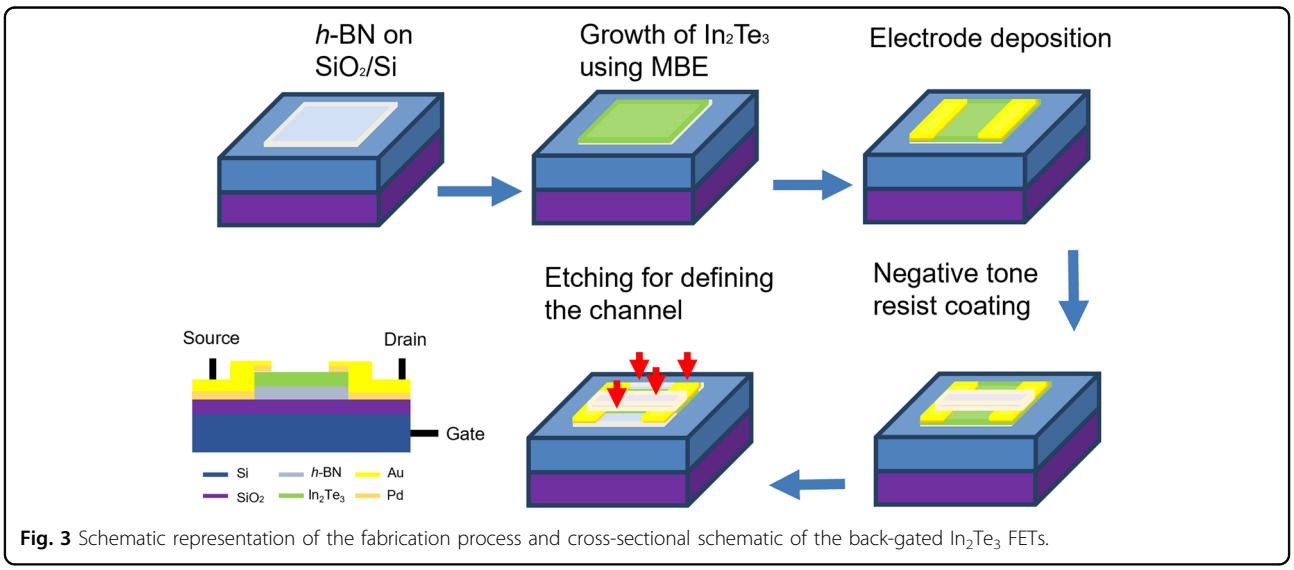

Fig. 3 Schematic representation of the fabrication process and cross-sectional schematic of the back-gated In_2Te_3 FETs.

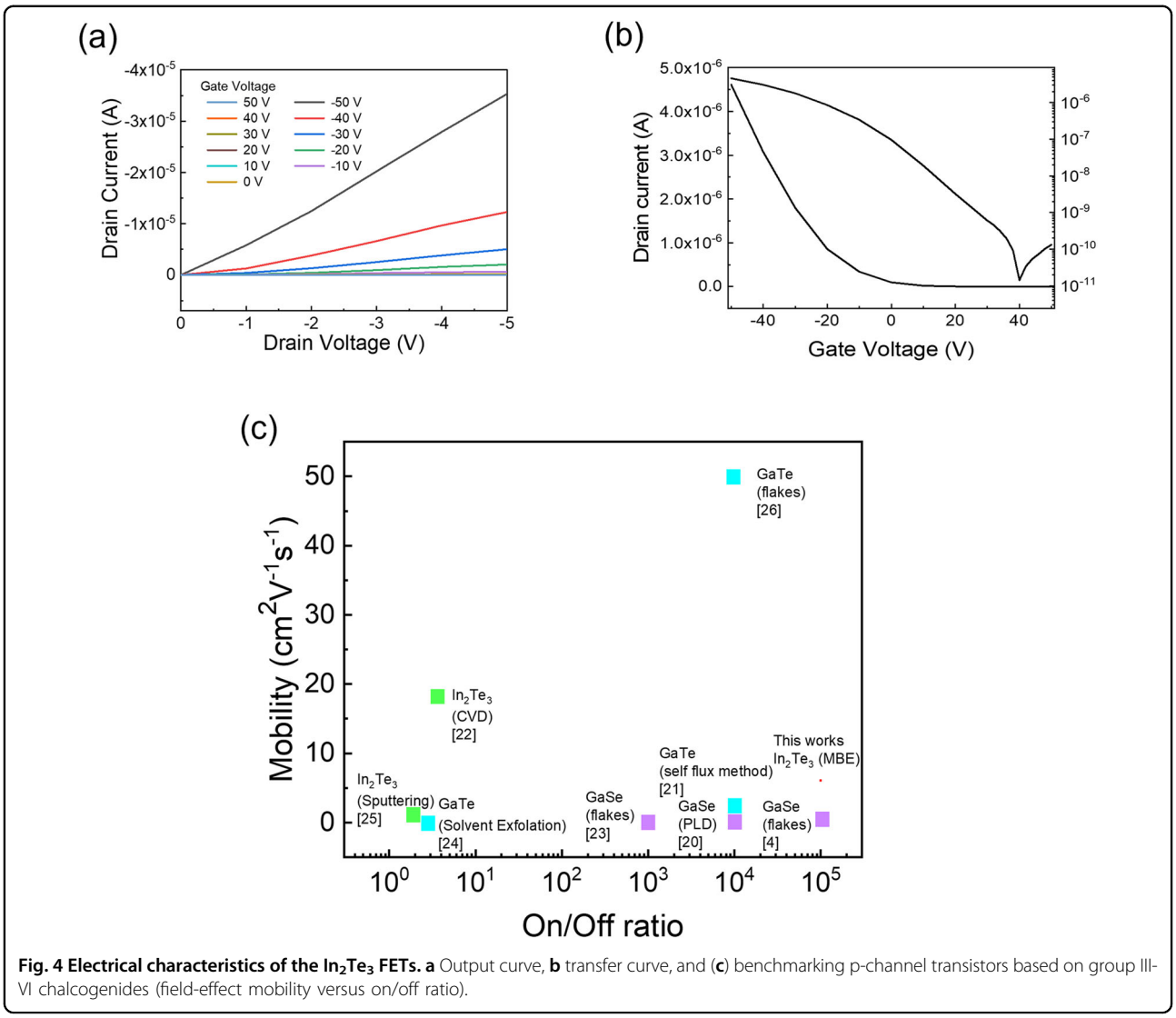

Fig. 4 Electrical characteristics of the In_2Te_3 FETs. a Output curve, **b** transfer curve, and (**c**) benchmarking p-channel transistors based on group III-VI chalcogenides (field-effect mobility versus on/off ratio).

As illustrated in Fig. 3, these In_2Te_3 thin films grown on *h*-BN were utilized for electronic device fabrication. Initially, Pd/Au bilayer contacts were deposited on In_2Te_3/*h*-BN using e-beam evaporation to form ohmic contacts. The channel was subsequently defined through reactive ion etching (RIE) with chlorine gas, employing a negative tone resist.

The electrical characteristics of the back-gated In_2Te_3 field-effect transistors (FETs) were evaluated by measuring the gate bias (V_{gs})-dependent current (I_{ds}) curve. Typically, the back-gated In_2Te_3 FETs are on, and as V_{gs} increases, I_{ds} decreases. The threshold voltage is identified as $V_{gs} = -10$ V, at which point the device is turned off (Fig. 4a). The output characteristics demonstrate that the back-gated In_2Te_3 FETs function as typical *p*-channel FETs. Unlike conventional FETs, no I_{ds} saturation is observed, suggesting that traditional channel pinch-off and channel length modulation do not occur. The current gradually decreases as the gate voltage increases according to the V_{gs}–I_{ds} curves for a V_{ds} of 1 V (Fig. 4a). These transfer characteristics indicate typical *p*-channel FET behavior and operation in depletion mode. As V_{gs} increases, the current decreases drastically to approximately 10^{-10} A above −16 V, which is the threshold voltage (V_{th}) of the back-gated In_2Te_3 FETs. A high I_{max}/I_{min} ratio of 10^5 was observed.

Another important indicator of transistor performance is transconductance ($g_m = dI_{ds}/dV_{gs}$), which peaks at maximum values close to the subthreshold region at 28 nS μm^{-1} when V_{ds} is set to 1 V. The peak field-effect mobility, determined from the transconductance in the linear regime ($V_{ds} = 1$ V), was measured to be 6.07 $cm^2 V^{-1} s^{-1}$, which is higher than that in previous works. The subthreshold swing was 6 V dec^{-1}, and the gate leakage current was 10^{-10} A (Fig. 4b). Compared with other *p*-channel transistors fabricated using various methods and

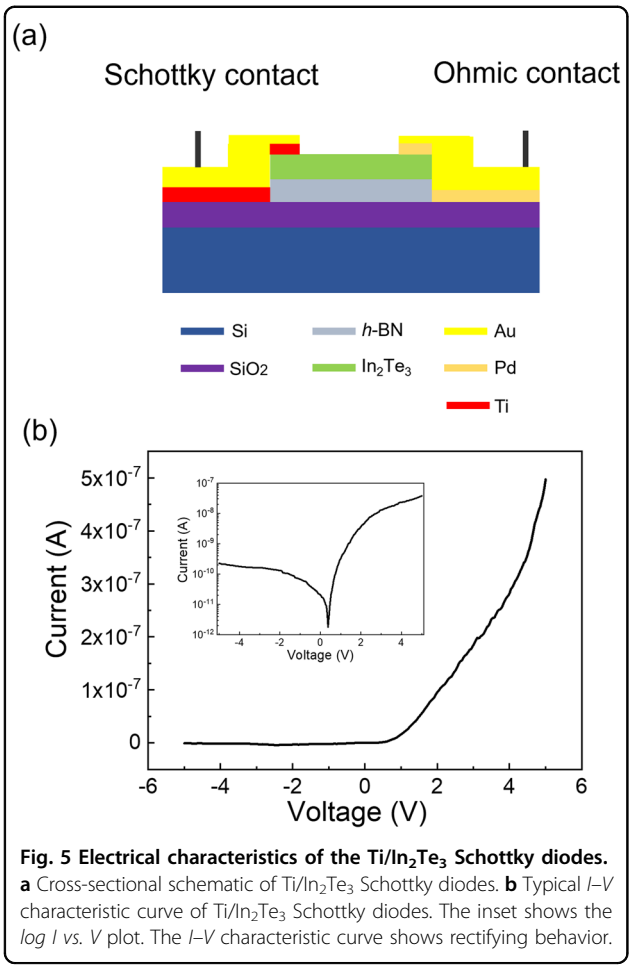

Fig. 5 Electrical characteristics of the Ti/In_2Te_3 Schottky diodes. **a** Cross-sectional schematic of Ti/In_2Te_3 Schottky diodes. **b** Typical *I–V* characteristic curve of Ti/In_2Te_3 Schottky diodes. The inset shows the *log I vs. V* plot. The *I–V* characteristic curve shows rectifying behavior.

materials from the group III-VI chalcogenide family, the MBE-grown In_2Te_3 from the current study, demonstrates enhanced performance, making it more suitable for switching devices (Fig. 4c).

Furthermore, In_2Te_3 Schottky diodes were fabricated for potential applications in logic circuits alongside FETs. To evaluate their electrical properties, the *I–V* characteristics of the Ti/In_2Te_3 Schottky diodes were measured, which formed a metal/semiconductor Schottky junction with a titanium (Ti) electrode (Fig. 5a). The *I–V* characteristic curve of the Ti/In_2Te_3 Schottky diodes shows a turn-on voltage of 1.34 V and a breakdown voltage of −3 V (Fig. 5b). The observed rectifying behavior is attributed to the formation of a Schottky contact between the low work function of titanium (4.33 eV) and the p-type semiconductor behavior of In_2Te_3. Typical *I–V* characteristics of Schottky diodes can be described by the following equation:

$$I = I_s \exp(qV/nk_BT - 1)$$

where, k_B is the Boltzmann constant, n is the ideality factor, T is the absolute temperature, and I_s is the saturation current of the diodes. From the *I–V* curves, the rectification ratio, ideality factor, and Schottky barrier height values were measured to be 514, 26.7, and 0.68 eV, respectively. These results demonstrated enhanced performance compared with previously reported group III-VI chalcogenide-based Schottky diodes with lower reverse-bias leakage currents[16–21], as shown in Table 1. This performance suggests that the diode can reliably function under reverse current flow, making it suitable for applications that demand minimal leakage, such as high-frequency device applications.

Table 1 Comparison of Schottky diode performances for *p*-channel group III–VI chalcogenides.

Diode	Barrier Height (eV)	Ideal factor (*n*)	Saturation current (A)	Ref.
Ti/In_2Te_3	0.68	26.7	0.4×10^{-9}	This work
Al/In_2Te_3	0.687	4.085	5.28×10^{-5}	16
Al/GaTe	0.61	2.5	N/A	17
Cd/GaTe	0.69	1.25	N/A	18
Mo/GaTe	0.58	1.1	N/A	19
Sn/GaTe	0.55	1.03	N/A	20
Au/GaSe	0.79	1.7	N/A	21
Au/GaSe: Ce	0.83	1.34	8.0×10^{-8}	21

Conclusions

We have successfully fabricated *p*-channel FETs and Schottky diode based on MBE-grown In_2Te_3. The two-step growth strategy employed resulted in full-coverage, atomically smooth In_2Te_3 films. In_2Te_3 films grown on *h*-BN substrates were shown to have atomically clean interfaces by employing MBE for precise control over the composition and phase. The electrical characteristics of the MBE-grown In_2Te_3 FETs, including enhanced mobility, reduced subthreshold swing, and a highly improved on/off ratio, were significantly improved. Additionally, the *I–V* characteristics of the Ti/In_2Te_3 Schottky diodes showed a low saturation current and higher barrier height than those of previous In_2Te_3-based diodes. The high on-off ratio of the *p*-channel FETs and the low saturation current of the Schottky diodes increase the versatility and potential for group III-VI chalcogenide-based integrated circuits. These characteristics make MBE-grown In_2Te_3 FETs and Schottky materials useful in logic devices. We believe that this approach for preparing high-quality group III-VI chalcogenide thin films is promising for next-generation electronics.

Acknowledgements
This work was financially supported by the National Research Foundation (NRF) of Korea (NRF-2021R1A5A1032996) and the Science Research Center (SRC) for Novel Epitaxial Quantum Architectures. This research was also supported by the Basic Science Research Program through the NRF funded by the Ministry of Education (2021R1A6A1A10044154), NRF-2022R1A2C3007807, and NRF-2019M3D1A1079215. Additionally, we also acknowledge the Brain Korea 21-Plus Program, the Institute of Applied Physics (IAP). Research Institute of Advanced Materials (RIAM) at Seoul National University.

Author details
[1]Department of Physics and Astronomy, Institute of Applied Physics, Seoul National University, Seoul, South Korea. [2]Department of Material Science Engineering and Research Institute of Advanced Materials, Seoul National University, Seoul, South Korea. [3]Interdisciplinary Program in Neuroscience, College of Science, Seoul National University, Seoul, South Korea. [4]Department of Physics and Department of Intelligent Semiconductors, Soongsil University, Seoul, South Korea

Author contributions
Imhwan Kim: Conceptualization, methodology, investigation, data curation, formal analysis, writing-review & editing, writing-original draft. Jinseok Ryu: Methodology. investigation & analysis. Eunsu Lee: Methodology & investigation. Sangmin Lee. : Methodology, investigation. Seokje Lee: Methodology & writing-review & editing methodology, investigation. Wonwoo Suh: Investigation & analysis. Jamin Lee: Investigation, writing-review & editing. Miyoung Kim: Conceptualization, funding acquisition. Hong seok Oh: Conceptualization, writing-review & editing. Gyu-Chul Yi: Writing—original draft, formal analysis, conceptualization, project administration, funding acquisition.

Conflict of interest
The authors declare no competing interests.

Publisher's note
Springer Nature remains neutral with regard to jurisdictional claims in published maps and institutional affiliations.

Supplementary information The online version contains supplementary material available at https://doi.org/10.1038/s41427-024-00578-0.

Received: 29 May 2024 Revised: 29 May 2024 Accepted: 14 October 2024.
Published online: 22 November 2024

References

1. Si, M. et al. A ferroelectric semiconductor field-effect transistor. *Nat. Electron.* **ume 2**, 580–586 (2019).
2. Sucharitakul, S. et al. Intrinsic electron mobility exceeding 10^3 $cm^2/(V\ s)$ in multilayer InSe FETs. *Nano Lett.* **15**, 3815–3819 (2015).
3. Jiang, J. et al. Stable InSe transistors with high-field effect mobility for reliable nerve signal sensing. *npj 2D Mater. Appl.* **3**, 1–8 (2019).
4. Dattatray Late, C. J. et al. GaS and GaSe ultrathin layer transistors. *Adv. Mater.* **24**, 3549–3554 (2012).
5. Saroj, R. K. et al., Photodetector arrays based on MBE-Grown GaSe/Graphene Heterostructure. *Adv. Opt. Mater.* **10**, (2022).
6. Wang, Z., Safdar, M., Jiang, C. & He, J. High-performance UV-visible-NIR broad spectral photodetectors based on one-dimensional In_2Te_3 nanostructures. *Nano Lett.* **12**, 4715–4721 (2012).
7. Yao, J., Deng, Z., Zheng, Z. & Yang, G. Stable, fast UV-Vis-NIR photodetector with excellent responsivity, detectivity, and sensitivity based on α-In_2Te_3 films with a direct bandgap. *ACS Appl Mater. Interfaces* **8**, 20872–20879 (2016).
8. Jacobs-Gedrim, R. B. et al. Extraordinary photoresponse in two-dimensional In_2Se_3 nanosheets. *ACS Nano* **8**, 514–521 (2014).
9. Afifi, M. A., Hegab, N. A. & Bekheet, A. E. The switching phenomenon in amorphous In,Te, thin films. *Vacuum* **47**, 265–269 (1996). (1996).
10. Zhen, J. et al. Superconductivity in In_2Te_3 under compression induced by electronic and structural phase transitions. *J. Phys. Chem. Lett.* **13**, 1226–1233 (2022).
11. Shi, X., Cho, J. Y., Salvador, J. R., Yang, J. & Wang, H. Thermoelectric properties of polycrystalline and Anisotropic optical and thermoelectric properties of In_4Se_3 and In_4Te_3 Thermoelectric properties of bipolar diffusion effect on $In_4Se_{3-x}Te_x$ compounds. *Appl. Phys. Lett.* **96**, 162108 (2010).
12. Zhang, S. et al. Large area growth of few-layer In_2Te_3 films by chemical vapor deposition and its magnetoresistance properties. *Sci. Rep.* **9**, 10951 (2019).
13. Huangfu, Y. et al. Low temperature synthesis of 2D p-Type α-In_2Te_3 with fast and broadband photodetection. *Small* **20**, 2309620 (2024).
14. Lee, S., Kwon, Y. K., Kim, M. & Yi, G. C. Novel Polytype of III–VI Metal Chalcogenides nano crystals realized in epitaxially grown InTe. *Small* **20**, 2308925 (2024).
15. Deiseroth, H. J. & Müller, H. D. Crystal structures of heptagallium decatelluride, Ga_7Te_{10} and heptaindium decatelluride, In_7Te_{10}. *N. Cryst. Struct.* **210**, 57–58 (1995).
16. Donepudi, L., et al. Barrier inhomogeneities Of Al/p-In_2Te_3 thin film Schottky diodes, *J. Nano-and Electron. Phys.* **3**, (2011).
17. Bose, D. N. & Pal, S. Schottky barriers on anisotropic semiconductor GaTe. *Philos. Mag. B*, *75*, 311–318.
18. Cankaya, G. & Abay, B. Current-and capacitance-voltage characteristics of Cd/p-GaTe Schottky barrier diodes under hydrostatic pressure. *Semicond. Sci. Technol.* **21**, 124–130 (2006).
19. Gülnahar, M. & Efeolu, H. Multiple-barrier distribution behavior of Mo/p-GaTe fabricated with sputtering. *J. Alloy. Compd.* **509**, 7317–7323 (2011).
20. Duman, S., Gürbulak, B. & Şata, M. Analysis of temperature dependent current voltage characteristics of Sn/*p*-GaTe/In Shcottky diode. *Opt. Mater.* **125**, 112138 (2022).
21. Ertap, H., Kacus, H., Aydogan, S. & Karabulut, M. Analysis of temperature dependent electrical characteristics of Au/GaSe Schottky barrier diode improved by Ce-doping. *Sens. Actuators A: Phys.* **315**, 112264 (2020).